AIAA 80-0347R

Effects of Initial Boundary-Layer Thickness on Transonic Diffuser Flows

M. Sajben* and J. C. Kroutil†
McDonnell Douglas Corporation, St. Louis, Mo.

Transonic flows displaying self-induced fluctuations were explored in a two-dimensional diffuser for shock Mach numbers to 1.4 and for approach boundary-layer displacement thicknesses from 2 to 5.8% of throat height. Steady and fluctuating properties were measured, including positions of shock, separation, and reattachment. Boundary-layer effects were moderate below and weak above a shock Mach number of 1.3, contrary to expectations of strong dependencies. Surface pressure power spectra were bimodal, reflecting both shock motion (100-200 Hz) and shear-layer turbulence (300-6000 Hz). The peak frequency for the latter decreases in the streamwise direction and becomes comparable to the shock-related frequency near the end of the divergent duct section.

Nomenclature

B = δ_i^*/h_*, inlet blockage on top wall
C_f = skin-friction coefficient
C_{ps} = p_s/p_{t0}, wall pressure coefficient
f = frequency
h = channel height (top-wall y coordinate)
H = δ^*/θ, boundary-layer shape factor
ℓ = streamwise length of reversed flow region
M = Mach number
p = pressure
q = $\frac{1}{2}\rho u^2$, dynamic pressure
R = perfect gas constant (286.96 $m^2/s^2/K$)
Re_θ = Reynolds number based on core flow speed and θ
S = power spectral density
u = velocity
x,y = space coordinates ($x=0$ at throat, $y=0$ on bottom wall)
w = mass flow through model
δ^* = boundary-layer displacement thickness
ν = p_{t0}/p_{sv}, overall pressure ratio
Π = coefficient of wake component
θ = boundary-layer momentum thickness

Subscripts

b = boundary layer
c = core flow
d = separation (detachment)
e = exit station
E = equivalent incompressible (van Driest) profile
i = inlet station
r = reattachment
s = static
sw = shock, at top wall
sm = shock, 2.54 cm above bottom wall
t = total
v = exhaust station (vent)
0 = plenum chamber
$1,2,3$ = identifying pin rows (Fig. 3)
$*$ = throat

Superscripts

$\tilde{(\ )}$ = distance normalized by throat height ($h_* = 48.3$ mm)
$\hat{(\ )}$ = rms value of fluctuating component

Presented as Paper 80-0347 at the AIAA 18th Aerospace Sciences Meeting, Pasadena, Calif., Jan. 14-16, 1980; submitted July 10, 1980; revision received March 30, 1981.

*Principal Scientist, McDonnell Douglas Research Laboratories. Associate Fellow AIAA.

†Unit Chief, McDonnell Douglas Research Laboratories. Member AIAA.

Introduction

THE work described herein is part of a long-term, experimental investigation of unsteady, transonic flows in diffusers. The flows have the same dominant features as those in airbreathing, supersonic inlets, and the oscillations under study are generically related to such performance-limiting phenomena as dynamic inlet distortion and buzz. The flows also have many characteristics common with airfoil flows in buffet; the investigation thus both benefits from, and indirectly contributes to, the understanding of external, unsteady transonic flows.

Early investigations[1-4] have provided a detailed description of nominally two-dimensional diffuser flows for a range of shock strengths, up to $M_{sw} \simeq 1.4$, with a thin initial boundary layer. These studies showed that the flows display self-excited fluctuations under all test conditions. A sequence of characteristic flow patterns was also identified in terms of the shock and separation bubble configurations (Fig. 1).

The effort reported in this paper focused on the effects of varying the thickness of the boundary layer approaching the diffuser throat. A sequence of four inlet boundary-layer thicknesses (with no change in shape factor, H_i) was used to study both the time-mean and fluctuating properties of the corresponding flows.

Experimental Apparatus

Diffuser Model

The experiments were conducted in a diffuser model of area ratio 2.37, whose contours are shown in Fig. 2, and whose coordinates are given in Table 1. The model is essentially identical to the one used in the first, exploratory phase of this program[2] and also to the one used in a second study focused on time-dependent surface pressure and shock position fluctuations.[3] Both ends of the model are shaped as constant-area channels, considered convenient boundary conditions both experimentally and theoretically. Suitable locations within the constant-area segments were arbitrarily designated as inlet ($\tilde{x} = -1.66$) and exit ($\tilde{x} = 11.51$) stations; the segment between them constitutes the region of interest. The downstream end of the second constant-area segment will be referred to as exhaust.

The side and bottom walls were equipped with discrete suction slots designed to keep the flow as nearly two-dimensional as possible. Most of the slots were located upstream of the inlet and downstream of the exit station. Streamwise slots located along the top corners in the divergent section were found effective in minimizing three-dimensionalities. These slots were the only ones within the channel segment of interest. There was no mass removal anywhere on the curved top wall.

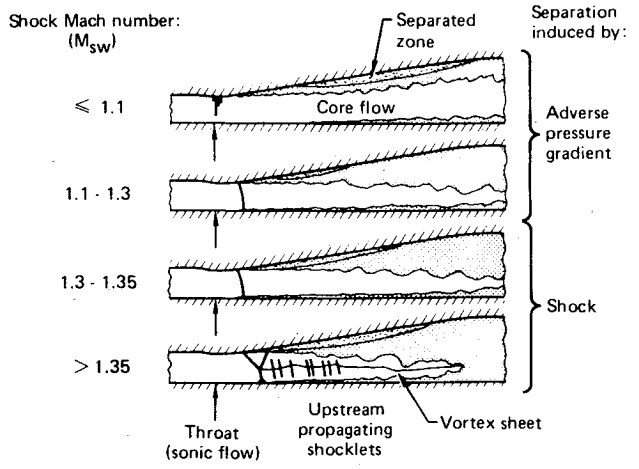

Fig. 1 Typical flow patterns.[2,3]

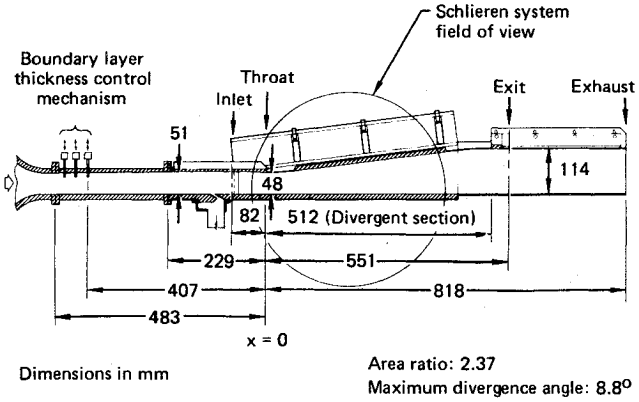

Fig. 2 Diffuser model.

The model was attached to a plenum chamber with a 25:1 contraction and was supplied with filtered, dry air at rates up to 2.2 kg/s. Maximum Reynolds number based on throat height and average throat conditions was 10^6. Test conditions were set by controlling plenum chamber pressure.

Boundary-layer displacement thickness was varied mechanically with three spanwise rows of round, cylindrical pins (Fig. 3). Each row formed a separate, comb-shaped assembly, whose teeth were inserted into the flow through a matching set of holes in the top wall. The immersion depths for each row could be varied independently up to 25 mm with micrometer screws. The last row of pins was located at $\tilde{x} = -7.90$, or 130-400 displacement thicknesses upstream of the throat, depending on δ_i^*.

Instrumentation

Flow rate to the model was measured by a choked Venturi meter, and the total of all flows removed through the suction slots was independently measured with another, subcritically operated Venturi meter.

Time-mean wall static pressure distributions on both top and bottom walls were measured using 0.4-mm diam wall orifices connected to two 48-channel scanivalves, each housing a ±34 kPa transducer (Druck model PECR-22). The same scanivalves were used to sense total pressures at the exit station from a total-pressure tube rake composed of 21 probes (0.4-mm i.d. and 0.8-mm o.d.). The tubes were arranged in two staggered vertical rows, and the entire rake could be moved spanwise to obtain the total pressure distribution over the entire cross section (typically, $8 \times 21 = 168$ readings were obtained for each condition).

The optical system of the facility used two 51-cm diam concave mirrors with 320 cm focal length. The system was used in both shadowgraph and schlieren modes: 5500 frames/s movies were taken with a Hycam camera, and 20 ns duration spark photographs were obtained with a commercial 35 mm Nikon camera. The system also incorporated a 256-element, line-scan imaging camera, whose output was processed to yield a real-time, analog signal proportional to shock position.[4] The output from this system is proportional to the x coordinate of the intersection between the upstream edge of the shock image and a horizontal line 2.54 cm above the model floor.

Time-mean separation and reattachment locations were obtained with oil-flow techniques. Inlet station total pressure profiles were measured on the top wall at midspan using a miniature total pressure probe. Surface pressure fluctuations were measured with seven flush-mounted transducers (Kulite model CQL-080) mounted on the top wall surface at various locations. Total pressure fluctuations at the exit station were measured with six Kulite transducers mounted on a vertical rake at channel midspan.

Table 1 Top wall contour coordinates[a]

$\tilde{x}$	$\tilde{h}$	$\tilde{x}$	$\tilde{h}$
−10.000	1.053	1.386	1.119
−1.179	1.053	1.646	1.160
−0.916	1.051	1.969	1.210
−0.653	1.037	2.359	1.270
−0.477	1.021	2.749	1.331
−0.341	1.010	3.269	1.4112
−0.209	1.0038	3.789	1.492
−0.073	1.0001	4.439	1.593
0.0	1.0000	5.095	1.694
0.204	1.0026	6.129	1.855
0.335	1.0069	7.169	2.016
0.466	1.016	8.137	2.166
0.593	1.022	8.865	2.283
0.729	1.033	9.326	2.327
0.865	1.047	9.783	2.355
0.985	1.061	10.241	2.3676
1.188	1.088	10.704	2.3684
		16.941	2.3684

[a] All distances normalized by throat height, $h_* = 44.1$ mm.

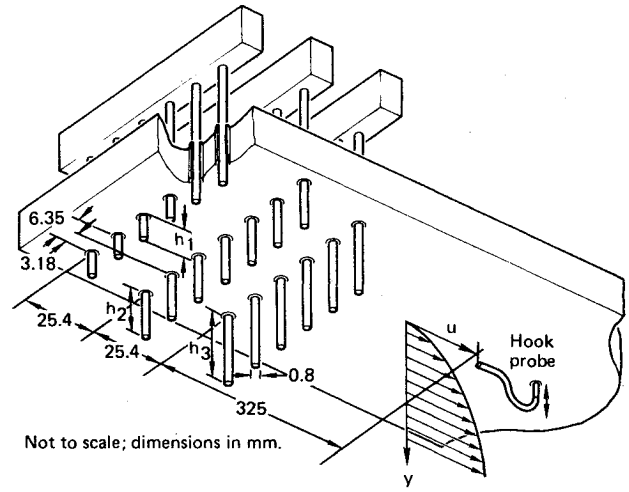

Fig. 3 Boundary-layer thickness control mechanism viewed from below.

Experimental Results

Test Parameters

The operating condition of the diffuser is most precisely characterized by the overall pressure ratio (ν), which unambiguously defined the state of the flow, stayed temporally steady despite the subsonic flow fluctuations, and could be controlled and measured to a high precision.

From the viewpoint of the physics of the flow, the time-mean shock strength (measured by the pre-shock Mach number) is a more meaningful independent variable. The precise measurement of this quantity is prohibitively difficult because of the large-amplitude shock oscillations; therefore, the Mach number was computed from the spatial minimum of the top wall static pressure distributions, assuming the local freestream pressure to be equal to the plenum pressure. This Mach number (M_{sw}) is a time-mean approximation to conditions existing at the edge of the top wall boundary layer just upstream of the shock. This Mach number controls the pressure rise experienced by the boundary layer and is an appropriate independent variable for describing boundary-layer behavior.

The experiments showed that the shock may be strongly curved or assume a lambda pattern, so that the shock strength may vary significantly in the vertical direction. This variation is described coarsely by a Mach number (M_{sm}) defined to approximate conditions near midchannel in the inviscid core flow. The shock position here (x_{sm}) is known from the line-scan system output, allowing the definition of M_{sm} as the supersonic Mach number associated with the area ratio $h(x_{sm})/h_*$, using one-dimensional, inviscid relations.

The critical parameter of this study is the inlet station, top wall boundary-layer thickness, referenced to the throat height. Following common usage in diffuser flow research, the quantity δ_i^*/h_* is referred to as blockage, B. This definition does not include contributions from the side and bottom wall boundary layers, and is, therefore, less than the total blockage. Unless indicated otherwise by appropriate superscripts, all flow property symbols designate time-mean values.

Inlet Conditions

Earlier tests in the same facility[1,2] established that the flow entering the model is uniform, parallel, and has a low turbulence level (~0.5%) outside the wall boundary layers. In addition, surface pressure fluctuations were measured in this test on the top wall near the inlet station. The fluctuation rms levels corresponded to those expected from the existing turbulent boundary layer. The diffuser throat is thus supplied with a flow free of appreciable spatial nonuniformities, containing only low-level fluctuations largely confined to the boundary layers.

Boundary-layer thickness at the inlet station was controlled within a 3:1 range using the pin assembly of Fig. 3. Immersions of the three pin rows were varied in an empirical trial-and-error process to produce a total of 33 inlet station total pressure profiles, determined by the miniature total pressure probe. Assuming that static pressure and total temperature at the probe tip were equal to the wall pressure and plenum chamber temperature, respectively, time-mean properties of the profiles were calculated.

The profiles were judged by the similarity of their van Driest transformed[5] versions to the constant-pressure, flat-plate profiles of Coles.[6] After detailed comparisons, four pin combinations were selected to form a sequence of increasing δ_i^*, while keeping the shape factor (H_i) constant at 1.52 within ±2%. These profiles are shown in Fig. 4, and Table 2 contains properties of both the original and the transformed profiles.

The contraction of the channel between the inlet station and the throat imposed a favorable pressure gradient on the boundary layer. The boundary-layer properties at the throat were computed using Cebeci's code[7] and the measured surface-pressure distributions, using the measured inlet profiles as initial conditions; results are included in Table 2. Throat conditions are more appropriate to the problem at hand; nevertheless, data are labeled by the directly measured inlet-station values.

The growth of the bottom and side wall boundary layers began at the sharp edges of suction slots located at $\tilde{x} = -2.5$ on the bottom wall and $\tilde{x} = -1.58$ on the side walls. By the evidence of schlieren spark photographs, the bottom layer was thin and laminar up to the shock, which appeared to trigger transition to turbulence. Profiles were not measured on the side and bottom walls.

Table 2 Inlet boundary layer properties[a]

Blockage (B)	0.020	0.028	0.040	0.058
Immersions, mm				
h_1	0.51	1.02	1.27	1.27
h_2	0.51	0.52	2.03	3.05
h_3	0.00	4.83	7.87	13.97
Core flow Mach number, M_c	0.769	0.775	0.783	0.799
Measured profile parameters				
H	1.53	1.50	1.54	1.52
$Re_\theta \times 10^{-3}$	11.6	16.5	22.9	34.0
Equivalent incompressible profile parameters[5]				
δ_E^*/h_*	0.0175	0.0245	0.0356	0.0511
H_E	1.294	1.261	1.297	1.271
$Re_{\theta E} \times 10^{-3}$	12.2	17.5	24.2	35.9
$C_{fE} \times 10^3$	2.92	2.89	2.5	2.38
Π_E	0.1	0.0	0.37	0.32
Incompressible profile parameters for $Re_{\theta E}$ by Coles[6]				
H	1.333	1.320	1.308	1.298
$C_f \times 10^3$	2.88	2.72	2.55	2.36
Properties at geometric throat				
Computed				
δ_*^*/h_*	0.0134	0.0154	0.0212	0.0312
H_*	1.57	1.69	1.67	1.65
$C_{f*} \times 10^3$	3.14	3.05	2.85	2.65
From choked flow rate				
δ_*^*/h_*	0.0108	0.0147	0.0192	0.0302

[a] Subscript i omitted in table.

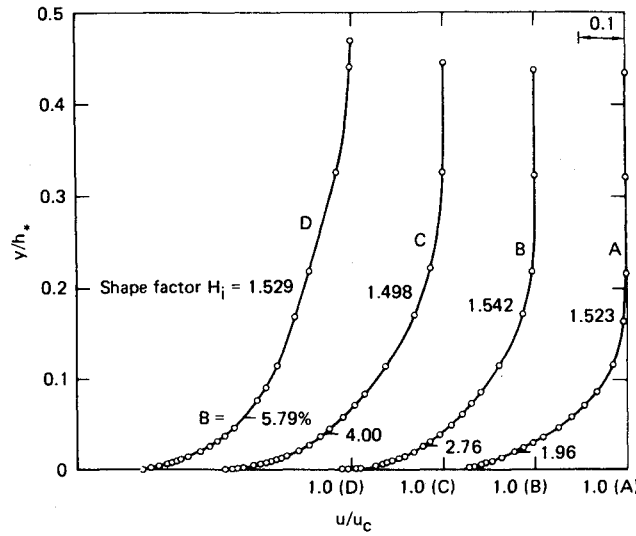

Fig. 4 Top wall boundary-layer profiles at the inlet station midspan.

Exhaust Conditions

The irregular eddying motion of the exhaust air in the test cell represented a flow perturbation imposed at the model exhaust. However, the associated pressure perturbation magnitude was at least two orders below the total pressure fluctuations found at the model exhaust and is therefore unlikely to exert a significant influence on the flow.

Time-Mean Flow Properties

The normalized mass flow ($\tilde{w}$) vs pressure ratio (ν) characteristics of the diffuser are shown as the top four curves of Fig. 5, where $\tilde{w}$ is the actual mass flow through the throat

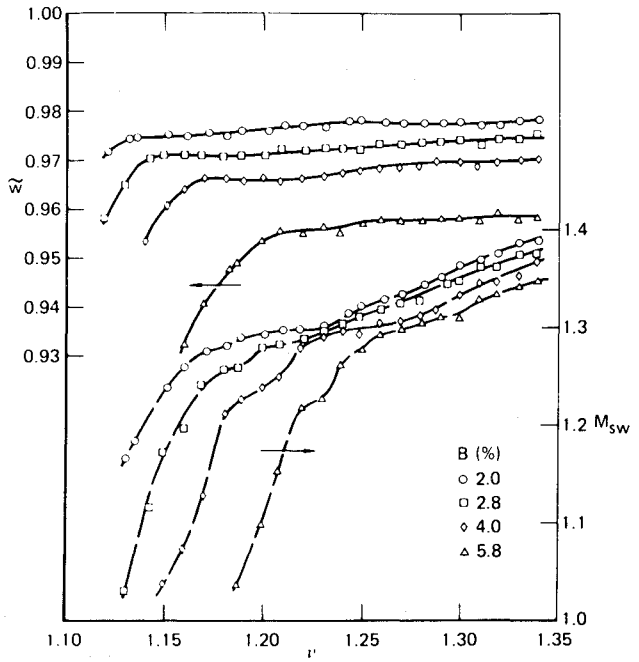

Fig. 5 Normalized mass flow and shock Mach number vs overall pressure ratio. Continuous lines are associated with left scale, dashed lines with right.

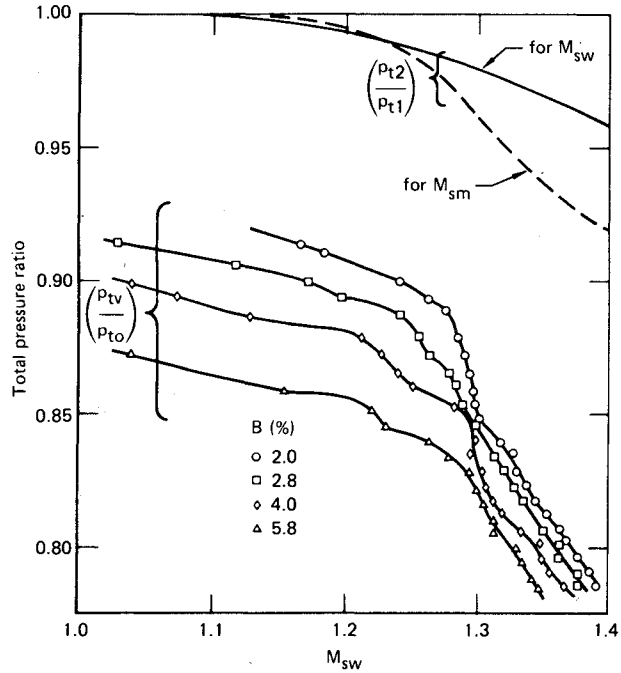

Fig. 7 Total pressure loss associated with a normal shock (top two curves) compared with measured total pressure recovery.

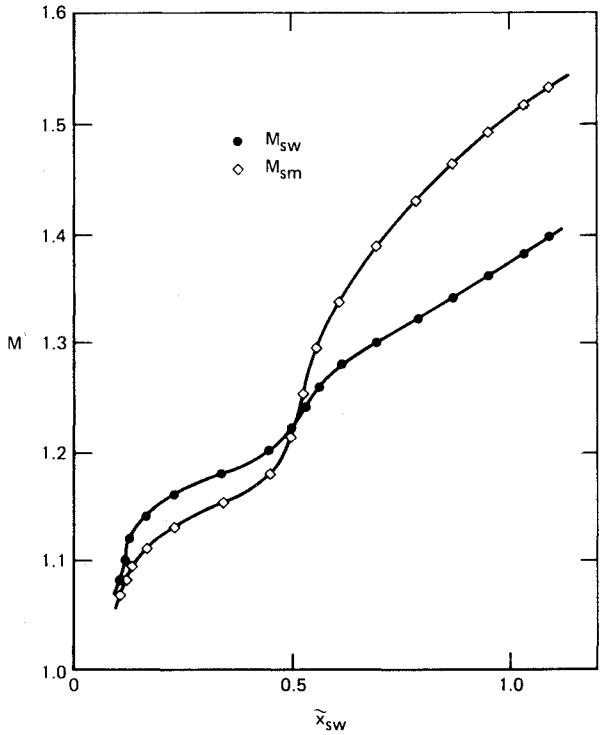

Fig. 6 Comparison of Mach numbers near top wall (M_{sw}) and at midchannel (M_{sm}).

normalized by the mass flow computed from the actual plenum chamber conditions and the geometrical throat area, using one-dimensional relations. For a real, choked flow, $\tilde{w}$ is less than unity because of the boundary-layer displacement effect at the throat. The deviation allows the estimation of B_* in a simple manner,[8] yielding δ_*^* values that are in excellent agreement with computations using the Cebeci code (Table 2).

The bottom curves of Fig. 5 show the top wall shock strength (M_{sw}) variations with ν. These curves were used to replace ν as an independent variable by M_{sw} in the remaining figures of this paper. The peculiar flattening of the curves at $M_{sw} \simeq 1.3$ is associated with the onset of shock-induced separation. Mass flow saturation occurs only after the shock becomes reasonably strong ($M_{sw} > 1.2$).

Figure 6 illustrates the vertical variations of shock strength by showing both M_{sw} and M_{sm} as functions of streamwise position. Near the throat, the convex wall curvature and the associated local acceleration of the flow increase the wall Mach number above the midstream value. Away from the throat, the shock assumes a lambda pattern such that the single-shock branch is positioned well downstream of the shock foot; therefore, $M_{sm} > M_{sw}$. As a consequence, there is a vertical variation of entropy in the postshock flow; however, this variation is small compared with the entropy increase experienced by the flow between the shock and exit station.

Figure 7 illustrates the ratio of exhaust and plenum total pressures as functions of shock strength and supports an important point concerning overall dissipation. (Exhaust total pressure was calculated from the known mass flow, total temperature, and static pressure at the exhaust station, using one-dimensional relations. The results given include losses caused by the boundary-layer control pins. Although these losses were not measured separately, two different estimates indicate that they are independent of M_{sw} and below 1%, even for the highest blockage.) Figure 7 shows that total pressure losses can be as high as 23% at $M_{sw} = 1.39$, whereas the normal shock relations for this Mach number yield only 4%; that is about one-sixth of the actual value. The shock loss is less than 8%, even if the greater strength of M_{sm} is used as a basis. It follows that the engineering practice of estimating the shock strength from the measured total pressure recovery using the Rankine-Hugoniot relations can be grossly misleading.

A joint morphology of the shock and the ever-present separation bubble is presented in Fig. 8, where data from three independent measurement methods are combined. The $\tilde{x}$ coordinates of the shock at the top wall and at the channel midheight are illustrated by the $\tilde{x}_{sw}$ and $\tilde{x}_{sm}$ curves. The two differ not only because the shock is curved or has a lambda shape, but also because of a systematic bias in the $\tilde{x}_{sw}$ measurement that yields data below the actual time-mean values. (The bias is proportional to the amplitude of the shock oscillation and is discussed in Ref. 2.) Data for both $\tilde{x}_{sw}$ and

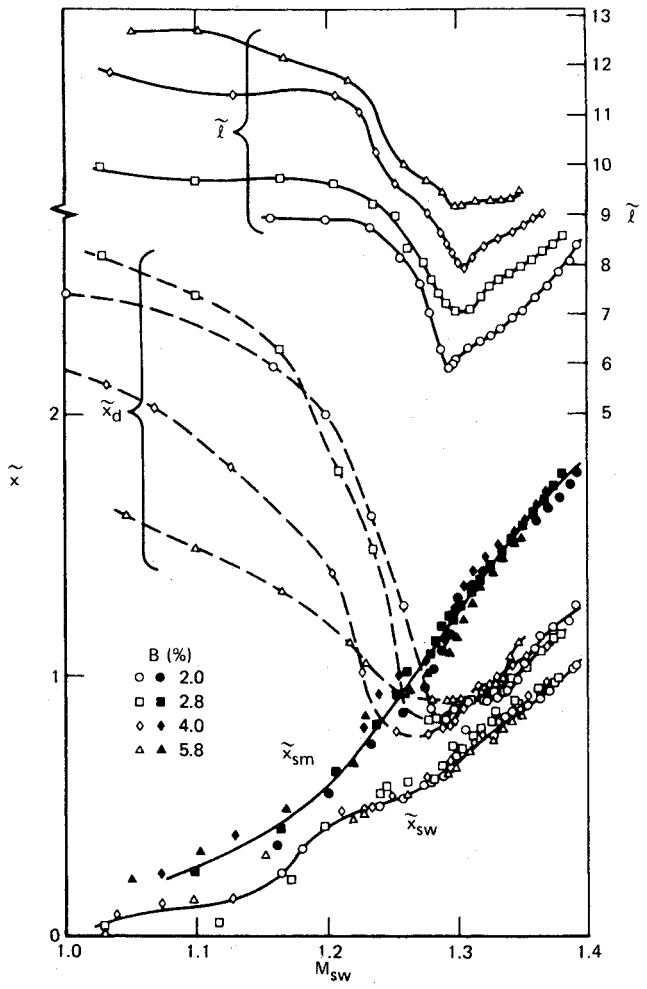

Fig. 8 Measured locations of shock position, separation, and reattachment points.

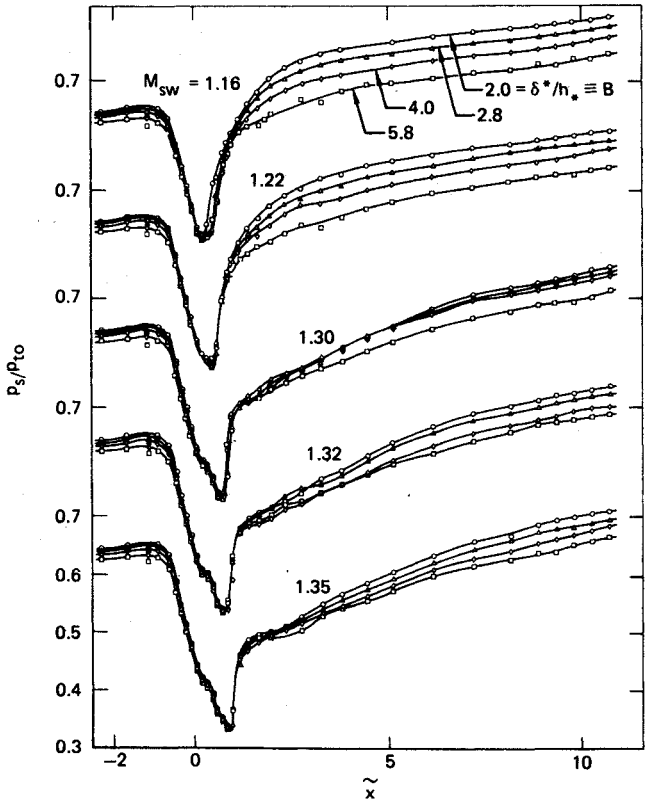

Fig. 9 Top wall, static pressure distributions for various blockage and shock-strength combinations.

$\tilde{x}_{sm}$ collapse into single curves for all blockage values, indicating that in the supersonic region the effective area distribution is not appreciably influenced by changing the initial boundary-layer thickness.

The remaining two families of curves in Fig. 8 describe the time-mean separation location and separation bubble length, with a measurement error of ±1.2 cm. Some scatter was removed by smoothing the data in their original $\tilde{x}_d(\nu)$ and $\tilde{x}_r(\nu)$ forms; the smoothed curves are within estimated error limits.

The $\tilde{x}_d$ data show that for weak shocks, separation occurs earlier as B increases. However, when the shock strength increases to $M_{sw} \cong 1.28$-1.3, the separation point moves to the shock location and becomes independent of blockage for shocks stronger than this limit. (The discrepancy between $\tilde{x}_{sw}$ and $\tilde{x}_d$ for $M_{sw} > 1.3$ is within the expected systematic experimental error.) This phenomenon is the onset of shock-induced separation; that is, the transition from subsonic, pressure-gradient-induced separation (PGIS) to shock-induced separation (SIS). This transition is accompanied by a major qualitative change in the character of most observable properties of the subsonic flow, including abrupt changes in trends. Some of the differences are illustrated on Fig. 8, others will be apparent in the figures that follow.

As shown by the top group of curves in Fig. 8, the length of the separation bubble increases with blockage. However, the bubble is almost as long as the entire divergent section, and its development must also depend significantly on the entire pressure distribution on the top wall. For reasons not understood, the bubble is always shortest when the PGIS-SIS transition occurs, i.e., when $M_{sw} \simeq 1.3$.

Figure 9 shows the streamwise distribution of top wall, time-mean, surface static pressures measured through orifices located near midspan. Some of the data were linearly interpolated to the M_{sw} values given to avoid a masking of blockage effects by concurrent, minor variations of M_{sw}, which are inevitable during actual runs. The data are not smoothed and were repeatable within 0.2%.

The character of the distribution shows a marked difference between those below and those above or including $M_{sw} = 1.3$. The change is clearly associated with the transition from one type of separation to another. For SIS, the pressure distributions show an abrupt break at separation, followed by a nearly linear variation over most of the divergent duct section.

As indicated by the spread of curves in a given M_{sw} = constant group, the pressure distributions are moderately sensitive to blockage in the PGIS mode and much less so in the SIS mode. Comparisons with available low-speed data for axisymmetric diffusers of similar area ratios[9] indicate that the sensitivity of our flows to blockage (even in the PGIS case) is much less than that found in incompressible diffuser flows.

The pressure rise across the shock is invariably well below that expected from a normal shock of strength M_{sw}. However, the observed pressure rises compare favorably with values for an oblique shock, using shock inclination angles taken from spark-schlieren photographs.

Detailed time-mean Mach number contour maps were constructed from exit station, total pressure rake data (included in Ref. 8). The maps illustrate that deviations between the data and fully two-dimensional flow are of the same order as measurement errors, at least over the center third of the spanwise extent. Consequently, the trends and magnitudes deduced from the data should apply to two-dimensional flows.

Fluctuating Flow Properties

The flow was unsteady under the range of conditions investigated, and the intensity and character of the fluctuations varied depending on the property in question and the combination of test parameters. The numerous high-speed films taken showed essentially the same features as those found in earlier tests.[2] Thickening the boundary layer seemed to increase the curvature of the shock slightly (when it was weak) and increase the distance of the bifurcation point from the top

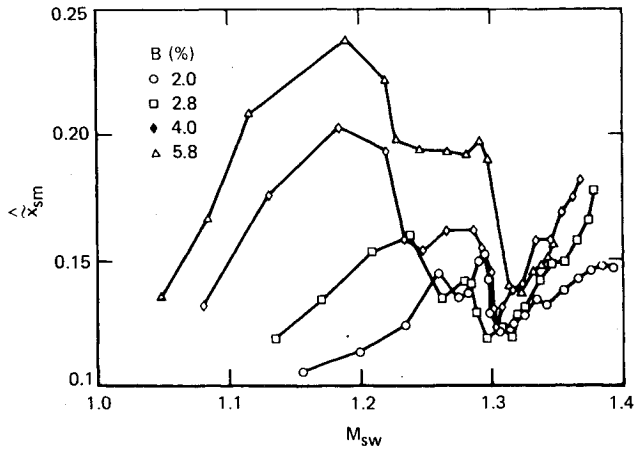

Fig. 10 Shock displacement rms values.

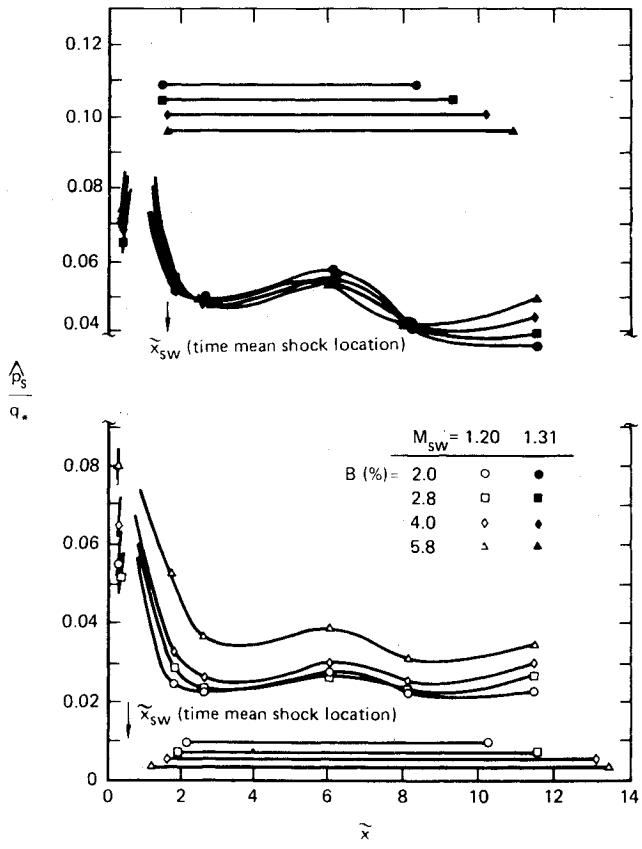

Fig. 11 Top wall, static pressure fluctuation rms distributions. Horizontal line segments show extent of separation bubble.

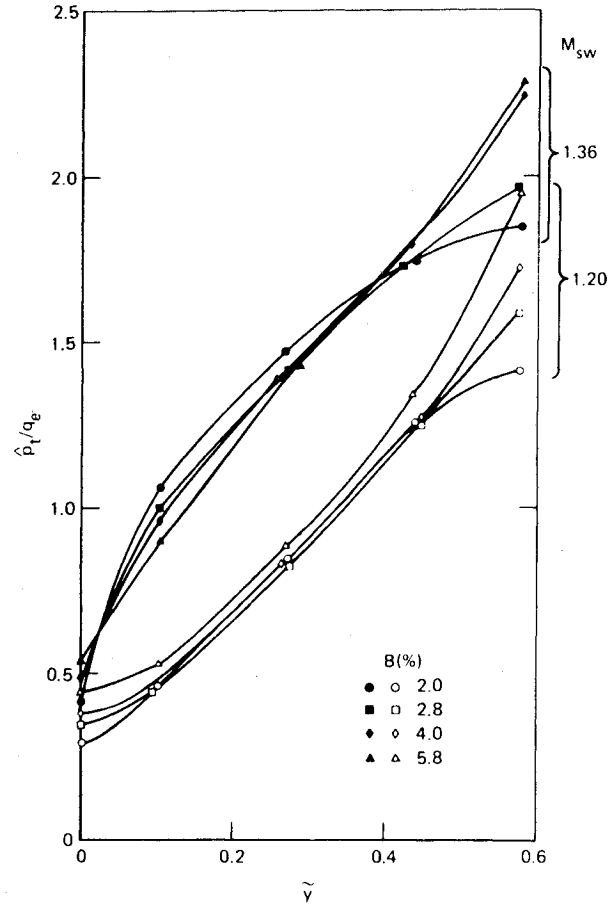

Fig. 12 Total pressure fluctuation rms intensities at the exit station midspan, as functions of distance from top wall. Data for $y=0$ were obtained by sensors flush-mounted on wall.

wall (when the shock was strong and lambda shaped). No other qualitative differences were noted.

The fluctuations were characterized quantitatively in terms of rms fluctuation intensities and by sets of power spectral density (PSD) distributions for the shock position and for static or total pressures sensed at various locations.

rms Distributions

The shock displacement amplitudes are given in Fig. 10. Points for identical B values are connected by straight lines; however, the precision of the measurement is around $\pm 2\%$ of h_*, and the fine structure of the curves is not likely to be significant. The main conclusion emerging from the plot is that the fluctuation amplitude is sensitive to blockage in the PGIS mode, but not in the SIS mode. At $M_{sw}=1.2$, the threefold increase of blockage more than doubled the displacement amplitude, whereas at $M_{sw}=1.37$, the corresponding increase is only one-third. Thus, the onset of shock-induced separation reduces the sensitivity of both time-mean and dynamic properties to B.

The rms values of the fluctuating wall static pressures are illustrated as streamwise distributions in Fig. 11 for two cases ($M_{sw}\simeq 1.2$, PGIS, and $M_{sw}\simeq 1.31$, SIS). The extent of the separation bubble is also given for each case. The distributions are similar to those found in earlier tests,[2] showing a high peak near the shock and a lower, but still intense fluctuation level in the divergent section. The maximum is sharp, and the expected peak values[3] around 0.16 are not detected because of insufficient spatial resolution. The postpeak $\hat{p}_s$ depends strongly on shock strength: it is nearly doubled by the relatively modest difference in Mach numbers between the two figures. Again, blockage effects are minor and significant only for the weak shock case.

Total pressure fluctuations at the exit station were determined by a rake of six high-response transducers located at midspan. Two of these showed unacceptably large differences in pre- and posttest calibrations, and the data had to be disqualified. The remaining data are illustrated in Fig. 12. The fluctuation amplitudes are again weakly dependent on blockage, but significantly dependent on shock strength. The $\hat{p}_t$ values increase with distance from the top wall, paralleling the increase in mean velocity. The fluctuations seem to involve large changes in velocity and only moderate changes in static pressure.

Reattachment occurred before the exit station in all but two of the cases shown in Fig. 12. The transducer nearest the top wall ($\tilde{y}=0.105$) was located within or at the edge of the separation bubble in these two cases ($B=4$ and 5.8%, both PGIS). No unusual fluctuation intensity or other anomaly is evident for such data.

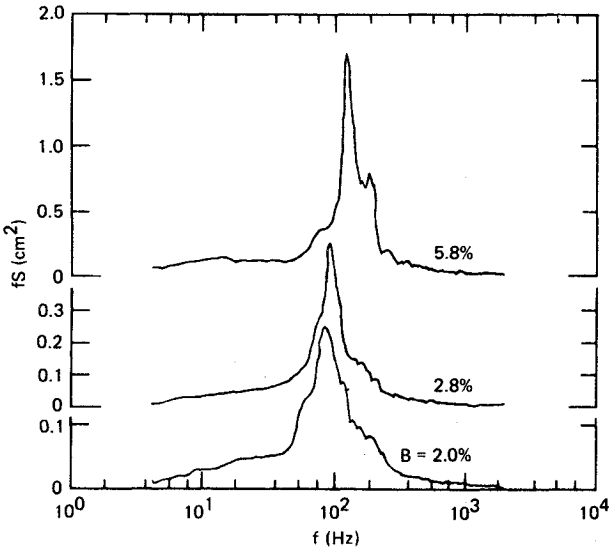

Fig. 13 Blockage effects on shock motion PSD. Weak shock ($M_{sw} = 1.2$).

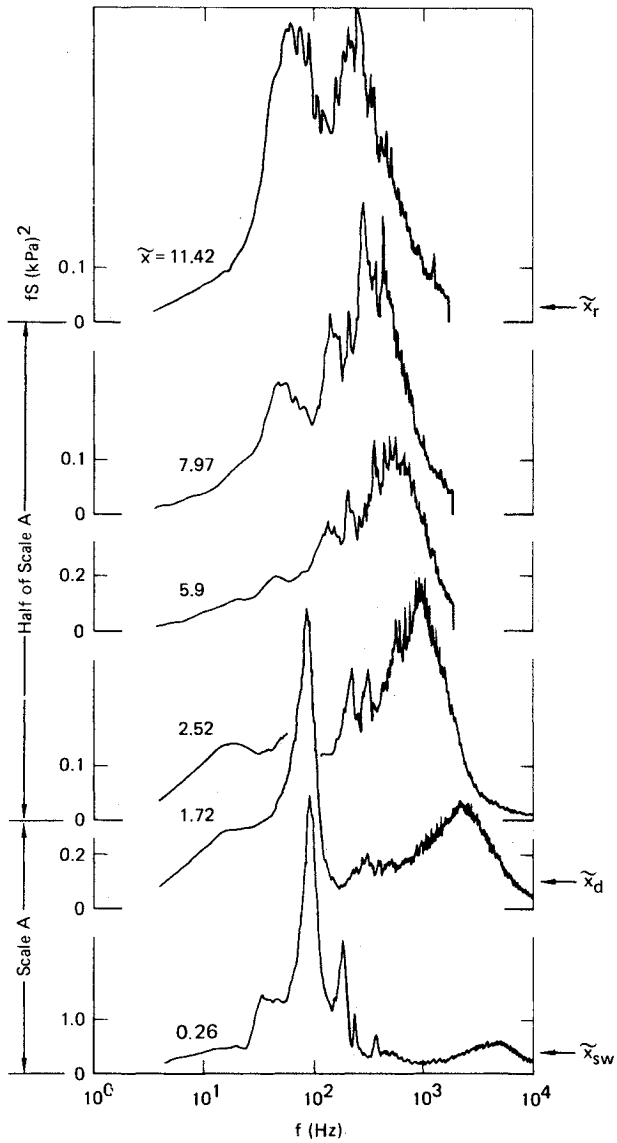

Fig. 14 Top wall pressure PSDs for $B = 2.8\%$, $M_{sw} = 1.20$. Vertical distances between successive horizontal axes are proportional to the respective distances between transducers. Factor of proportionality is halved for distances beyond $\tilde{x} = 2.52$.

Power Spectral Density Data

Perhaps the most interesting revelations came from the analysis of power spectral density (PSD) distributions, deduced from the fluctuating top wall pressure and the shock-position signals.

All spectra presented here are in the form of $fS(f)$ vs ℓnf plots, as opposed to the commonly used ℓnS vs ℓnf representation. The advantage of this choice of variables is that, unlike the usual log/log representation, the area under a given curve segment is linearly proportional to the contribution of the respective frequency range to the total fluctuating (rms) intensity. [$Sdf = (fS)\,(df/f) = (fS)\,d(\ell nf) \neq \ell nS\,d(\ell nf)$]. As a result, the dominant frequency ranges can be clearly recognized.

Figure 13 is a comparison of shock position PSDs for weak shocks, which illustrates the blockage effect. The spectra possess a well-defined, narrow-band peak which shifts toward higher frequencies with increasing blockage. The fluctuation magnitudes increase rapidly with B, as illustrated in the $\hat{x}_{sm}$ values of Fig. 10. In contrast, the character of shock displacement fluctuations is independent of B for strong shocks.

Figure 14 is a composite plot of six surface pressure PSDs, which are arranged to show their proper spatial relationships, as defined by the transducer locations. Despite the fine structure present in the PSDs, Fig. 14 illustrates two major, significant features. One is a sharp peak at the shock-displacement frequency ($f_{sm} \simeq 90$ Hz) that appears in spectra upstream of separation and downstream of reattachment, although in a somewhat broadened form in the latter case. This peak is almost completely suppressed in signals coming from transducers that are shielded from the core flow by the separation bubble.

The second major feature is a broad peak at higher frequencies. Near the shock location, the peak is at $f_b \simeq 5$ kHz. At locations farther downstream, the peak gradually shifts toward lower frequencies until it eventually occurs near the reattachment point at 300 Hz. This value is of the same order as the shock oscillation frequency.

There are strong reasons to believe that the second peak is associated with turbulence in the wall shear layer (which may or may not be attached at the transducer location). The first reason is that the frequency varies with x in the same way as the quantity δ^*/u_c, which is the scale expected for shear-layer turbulence frequencies. The core flow velocity (u_c) decreases while δ^* increases with x, and these two effects combine to produce the rapid decrease shown by the peak frequencies.

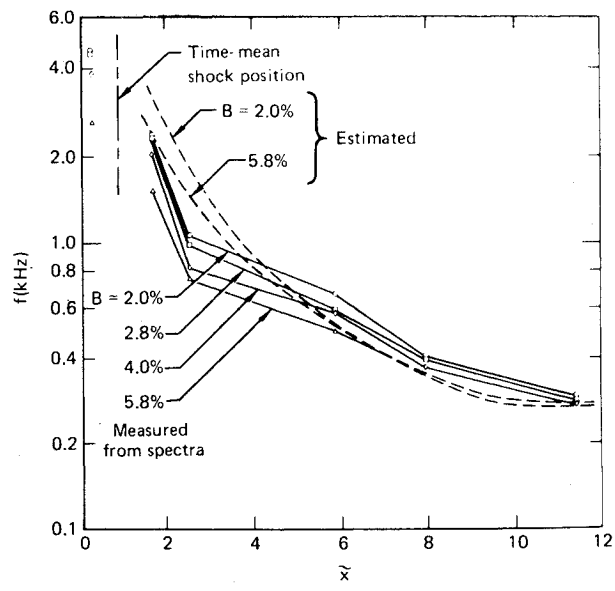

Fig. 15 Comparison of shear-layer frequencies taken from PSDs with estimates computed from time-mean data ($M_{sw} = 1.20$).

It is possible to obtain estimates of both δ^* and u_c from the available time-mean mass flow, cross-sectional area, static pressure, and total temperature data.[8] These estimates are compared with the peak frequencies in Fig. 15. The trends of the estimate, covering a frequency range of nearly 17:1, agree with the spectral data throughout most of the diffuser length.

The second reason lies in the dependence on blockage. Figure 15 shows the peak frequency variation for the four blockage values studied; f_b varies inversely with B as expected.

The third reason is that similar surface pressure, PSDs, obtained on the bottom wall of the diffuser in earlier tests under a much thinner, attached boundary layer,[3] did not show the shear-layer-related peaks discussed here.

The conclusion is that the turbulence in the rapidly thickening top wall boundary layer is associated with frequencies that decrease sharply in the streamwise direction and may, near the end of the divergent section, become low enough to become comparable to the shock-oscillation frequency. This conclusion implies that shear-layer turbulence may be an important (or even dominant) source of perturbations that are responsible for the self-induced fluctuations found in the system.

Space-time correlations of shock position and wall pressure fluctuation signals were calculated and examined to identify significant patterns similar to those reported in Ref. 3. The cross-correlation maps, however, were too complex to be interpreted with confidence. The bimodal PSD distributions suggest that the cause of this complexity is the presence of two different types of fluctuations which contribute almost equally to the overall fluctuation intensities. Since both types of perturbations can move both upstream and downstream, the situation is apparently beyond the resolving power of conventional correlation techniques.

Conclusions

The experimental results show that the influence of the approach boundary-layer thickness on nominally two-dimensional transonic diffuser flows depends on the shock strength.

If the Mach number before the shock is less than approximately 1.3, flow separation occurs well downstream of the shock, i.e., separation is induced by the adverse pressure gradient in the subsonic flow. In this situation, the boundary-layer thickness has a significant but moderate influence on both the time-mean and fluctuating flow properties. As B increases, separation occurs earlier, reattachment occurs later, static and total pressure recoveries are reduced, and the three-dimensional features of the flow are intensified. Shock displacement amplitudes increase dramatically, but frequencies increase only slightly. Surface pressure fluctuations change minimally.

Shock Mach numbers greater than 1.3 involve a pressure jump large enough to cause immediate separation. An increase of B under this condition generally will result in consequences similar to those for weak shocks. However, the magnitude of the effects is much smaller, and for several flow properties (e.g., surface pressure fluctuation) is virtually nil.

One valuable byproduct of this investigation was the experimental demonstration of earlier expectations that the wall pressure fluctuations are originating from two distinct mechanisms. One source is the shock oscillation and the associated pressure fluctuations that are coherent along the diffuser. This source accounts for a large, low-frequency contribution near 100 Hz. The second source is the local turbulence in the shear layer whose dominant frequency range varies widely along the flow from $\simeq$6000 Hz near the shock to $\simeq$300 Hz near the end of the divergent section. Except for low-frequency-dominated locations near the shock, the two contributions are of comparable intensity.

The turbulence frequencies near the duct end are sufficiently low to interact with the shock oscillation and are possibly the reasons for its presence. The present flows, therefore, contain large regions in which the difference between the time scales of turbulence and the time scale for the unsteady mean motion is small. The time-dependent description of flows in this class thus may require a model capable of describing at least some details of the large eddies in the flow. Theories on this level of sophistication are presently unavailable, and experimental exploration remains essential.

Acknowledgment

This work was sponsored by the Air Force Office of Scientific Research under Contract No. F49720-77-C-0082. The authors express their appreciation to Dr. Wilbur L. Hankey of the Air Force Flight Dynamics Laboratory for stimulating discussions about the causes of the observed oscillations.

References

[1] Sajben, M., Kroutil, J.C., and Chen, C.P., "A High-Speed Schlieren Investigation of Diffuser Flows with Dynamic Distortion," AIAA Paper 77-875, July 1977.

[2] Sajben, M., Kroutil, J.C., and Chen, C.P., "Unsteady Transonic Flow in a Two-Dimensional Diffuser," AGARD Conference Proceedings No. 227, *Unsteady Aerodynamics 1977,* pp. 13-1 to 13-14.

[3] Chen, C.P., Sajben, M., and Kroutil, J.C., "Shock-Wave Oscillations in a Transonic Diffuser Flow," *AIAA Journal,* Vol. 17, Oct. 1979, pp. 1076-1083.

[4] Sajben, M. and Crites, R.C., "Real-Time Optical Measurement of Time-Dependent Shock Position," *AIAA Journal,* Vol. 17, Aug. 1979, pp. 910-912.

[5] van Driest, E.R., "Turbulent Boundary Layer in Compressible Fluids," *Journal of the Aeronautical Sciences,* Vol. 18, March 1951, pp. 145-160, 216.

[6] Coles, D., "The Problem of the Turbulent Boundary Layer," *Zeitschrift fuer Angewandter Mathematik und Physik,* Vol. 5, 1954, pp. 151-162.

[7] Cebeci, T. and Smith, A.M.O., *Analysis of Turbulent Boundary Layers,* Academic Press, N.Y., 1974, Chaps. 7-9.

[8] Sajben, M. and Kroutil, J.C., "Effects of Approach Boundary Layer Thickness on Oscillating Transonic Diffuser Flows Including a Shock," AIAA Paper 80-0347, Jan. 1980.

[9] Sajben, M., Kroutil, J.C., and Sedrick, A.V., "Conical Diffuser Flows with Natural and Screen-Simulated Inlet Conditions," *AIAA Journal,* Vol. 14, Dec. 1976, pp. 1723-1730.